Nano Research

Open Access

Research Article

Non-close-packed 2D AuNP arrays via point-to-point adsorption on a block copolymer micelle monolayer for nano-floating gate memory

Changxu Liu[1], Haihong Chen[2], Shuai Deng[1], Wang Li[1], Xi Mao[1], Wen Li[2] ✉, Mingdong Yi[2], Renhua Deng[1] ✉, and Jintao Zhu[1] ✉

[1] *Key Laboratory of Materials Chemistry for Energy Conversion and Storage of Ministry of Education (HUST), and State Key Laboratory of Materials Processing and Die & Mold Technology, School of Chemistry and Chemical Engineering, Huazhong University of Science and Technology (HUST), Wuhan 430074, China*

[2] *Key Laboratory for Organic Electronics and Information Displays Institute of Advanced Materials (IAM), Nanjing University of Posts & Telecommunications, Nanjing 210023, China*

Cite this article: *Nano Research*, **2026**, *19*, 94908645. https://doi.org/10.26599/NR.2026.94908645

ABSTRACT: Non-close-packed (NCP) two-dimensional (2D) ordered nanoparticle (NP) arrays have attracted considerable attention due to their unique properties; however, their efficient and large-scale fabrication remains challenging. In this study, we present a facile yet effective point-to-point adsorption method for producing large-area NCP 2D ordered gold NP (AuNP) arrays using a rapidly assembled block copolymer (BCP) micelle monolayer as a template. By capitalizing on the inherent monodispersity and soft corona characteristics of BCP micelles, combined with the industrial compatibility of dip-coating technology, we achieved efficient and scalable fabrication of ordered BCP micelle monolayers. Key processing parameters, including dip-coating speed, micelle concentration on morphology of the templates, were systematically optimized. These micelle-monolayers serve as templates for the point-to-point adsorption of AuNPs, resulting in well-defined NCP 2D arrays. Adsorption mechanism was revealed to be an electrostatic interaction between protonated P4VP cores and size-matched AuNPs stabilized by citrate. The fabricated AuNP arrays demonstrate high performance in nano-floating-gate transistor memory devices, exhibiting a memory window of 54 V, on/off ratio of 3.8 × 10^3, and endurance stability over 110 write-read-erase-read cycles. These performance metrics significantly surpass those of conventional BCP-only templates, which showing great promise for applications in optoelectronic devices.

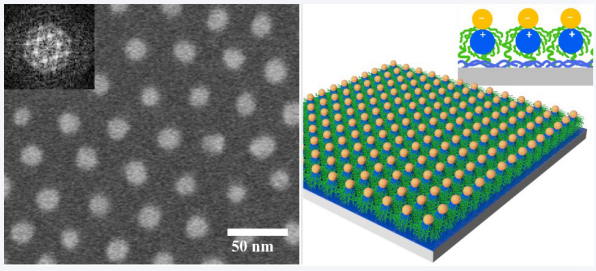

KEYWORDS: block copolymer (BCP), self-assembly, micelles, dip-coating, nanoparticle arrays, nano-floating-gate memory

1 Introduction

Ordered yet non-close-packed (NCP) two-dimensional (2D) nanoparticle (NP) arrays are of significant functional importance across multiple application domains [1], including charge-trapping memory devices [2–8], anti-reflective coatings, biological sensing [9–12], photodetectors [13]. For example, NCPs with relatively wide photonic band gaps are highly suitable for optoelectronic devices, such as light-emitting diodes and optical switches [14, 15]. The spatially isolated structural units effectively prevent crosstalk between individual functional components, a critical feature that enhances their performance in high-density data storage [16]. Furthermore, the discrete arrangement of NPs not only facilitates higher-density information storage but also helps suppress lateral leakage currents, properties that have been extensively leveraged in nanoscale floating-gate memory devices [17, 18]. Therefore, developing efficient fabrication methods for large-area NCP 2D NP arrays is of great desirability.

Compared to close-packed 2D architectures, NCP configurations generally demand more intricate fabrication strategies [13, 19–21]. The primary challenge in constructing NCP 2D NP arrays lies in the precise control of interparticle spacing and ensuring long-term structural stability. The top-down techniques, such as electron beam lithography [22] and dip-pen lithography [23], show high precision in fabrication of NP arrays; however, these approaches require special expensive equipment. The bottom-up assembly has emerged as a promising solution, enabling the fabrication of arrays

Received: February 7, 2026; **Revised:** March 12, 2026
Accepted: March 16, 2026

✉Address correspondence to Renhua Deng, rhdeng@hust.edu.cn; Wen Li, iamwli@njupt.edu.cn; Jintao Zhu, jtzhu@mail.hust.edu.cn

with tunable interparticle distance [24]. For example, we have reported the preparation of AuNP arrays via interfacial assembly [4, 5]. This approach is fundamentally based on particle close-packing; however, by modifying the NP surfaces with polymeric ligands, non-close-packed arrangements of the NP cores are achieved indirectly. While these methods have led to notable improvements in spatial ordering, they typically require the modification of NP surfaces with polymer ligands at specific molecular weights and grafting densities [25–28]. Such functionalization may, however, compromise the intrinsic physical and chemical properties of the NPs, potentially limiting their performance in subsequent applications.

Employing templates featuring nanoscale chemical patterns or topological grooves allows direct deposition of NPs into NCP 2D NP arrays. Nevertheless, such techniques inevitably involve additional nanolithography processes, which increase fabrication complexity and cost [29–31]. Block copolymers (BCPs), composed of two or more polymer chains with distinct chemical properties linked by covalent bonds, are known for their ability to self-assemble into periodic nanostructures due to the thermodynamic incompatibility between their constituent segments [32–34]. Concurrently, the intrinsic properties of BCPs have been extensively utilized in fabricating nanoscale patterns with various microphase-separated architectures, including spherical, cylindrical, and lamellar morphologies [35–41]. These pattern structures serve as templates to guide the arrangement of NPs into ordered arrays on solid substrates. The ability to produce highly ordered NP arrays makes this method particularly appealing [40–43]. Nevertheless, most BCP-mediated fabrication protocols still require sequential pre- and post-processing steps to achieve patterned nanoparticle arrays [44–46]. These procedures typically involve substrate surface modifications to accommodate polymeric deposition, followed by essential BCP template optimizations such as crosslinking, etching, and thermal annealing [47–49]. Such multi-stage operations, while effective for morphology control, inevitably introduce extended processing durations, substantially compromising overall production efficiency. There remains a critical demand for developing streamlined, efficient, and precisely controllable fabrication strategies for NCP 2D NP arrays to holistically address the tripartite industrial requirements of scalability, cost-effectiveness, and manufacturing integration efficiency, thereby bridging the gap between laboratory-scale precision and production-line practicality.

Herein, we demonstrate a strategy for rapid fabrication of BCP pattern templates through self-assembly of spherical BCP micelles by a single-step dip-coating process. The self-assembled monolayers of micelles can serve as templates for NP arrays via point-to-point adsorption (Fig. 1). Spherical micelles of polystyrene-*b*-poly (4-vinyl pyridine) (PS-*b*-P4VP) spontaneously formed in tetrahydrofuran (THF), which can self-assemble into ordered monolayers. Large area ordered 2D AuNP arrays are fabricated through electrostatically adsorbing with the protonated P4VP core of micelles. Key processing parameters, including dip-coating speed, micelle concentration, size matching of micelle core with NP, and BCP molecular weight, were systematically optimized to ensure the formation of high-quality ordered arrays. We fabricated AuNP arrays exhibit exceptional performance as charge-trapping layers in nano-floating-gate memory devices.

2 Results and discussion

2.1 Method and mechanism for AuNP arrays via Micelle template

The self-assembled monolayer micellar templates were fabricated via a one-step dip-coating process from THF solutions of PS-*b*-P4VP with identical molecular weights. The solubility parameters for THF, PS, and P4VP are 18.6, 17.6, and 22.5 ($MPa^{1/2}$) [50], respectively. This indicates that THF is a good solvent for the PS block, while exhibiting relatively poor solvency for P4VP. Consequently, in solutions containing BCP at specific concentrations (e.g., 1 mg/mL, with the exact value dependent on molecular weight), spherical micelles with collapsed P4VP cores preferentially form. Dynamic light scattering (DLS) results (Fig. 2(a)) confirm the presence of micelles in solution, revealing a narrow size distribution with an average hydrodynamic diameter of D = 63.1 ± 0.029 nm, indicative of spherical morphology. This spherical micelle structure was further corroborated by TEM investigation (Fig. S1 in the Electronic Supplementary Material (ESM)), which determined the P4VP core diameter as D_{core} = 20.33 ± 0.14 nm. The observation of smaller aggregates suggests the presence of free polymer chains in the solution. Critically, for the PS-*b*-P4VP/THF system, a dynamic equilibrium exists between unimers (free polymer chains) and spherical micelles. As the solution concentration progressively approaches the critical micelle concentration (CMC) from above, the fraction of free BCP chains increases.

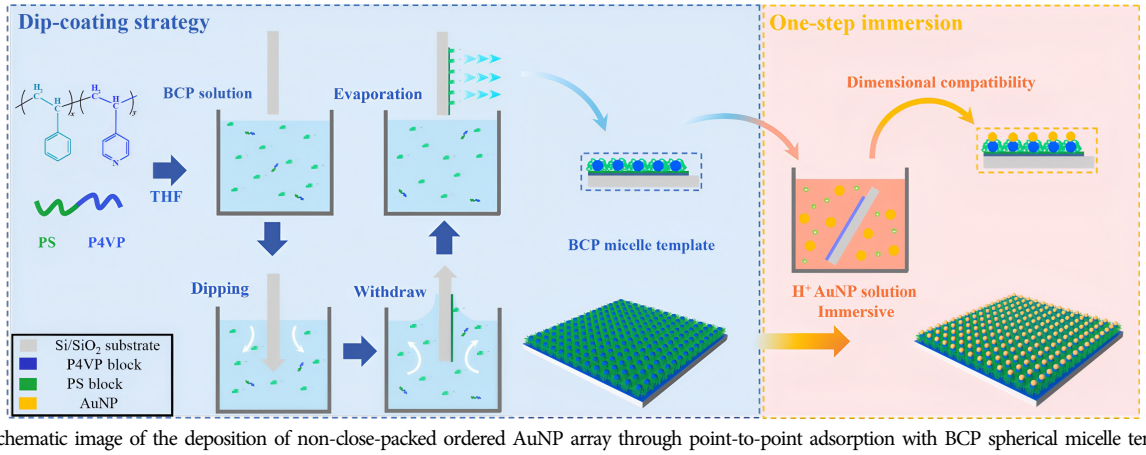

Figure 1 Schematic image of the deposition of non-close-packed ordered AuNP array through point-to-point adsorption with BCP spherical micelle templating via electrostatic interaction.

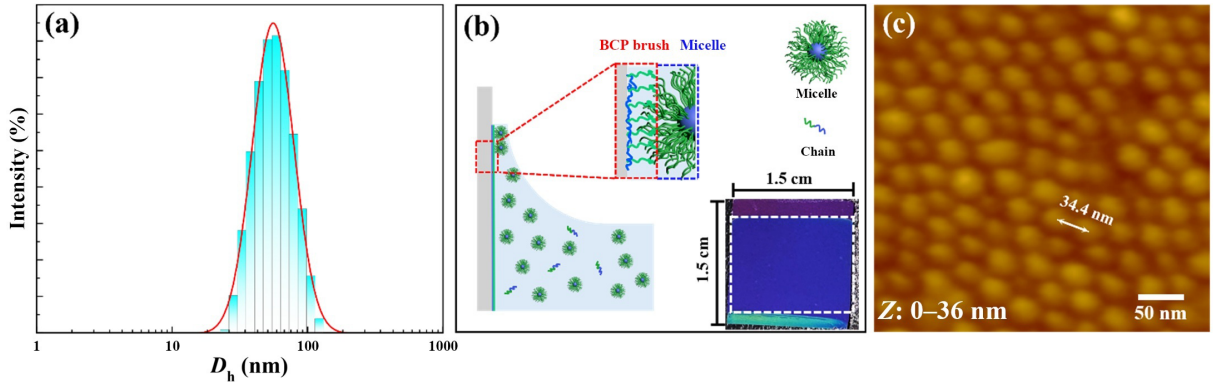

Figure 2 (a) The micelle diameter obtained by DLS. (b) The schematic diagram of BCP micelle template deposition, with the inset showing an optical micrograph of the fabricated micelle templates. (c) AFM height image of the micelle template, the annotation in (c) quantifies the statical distribution of inter-micelle center-to-center distance.

Figure 2(b) demonstrates the enhanced structural elucidation of the micellar template fabricated via dip-coating on substrates. Originating from the presence of free BCP chains in solution, substrate surfaces become initially populated by unbound polymer segments, with spherical micelles subsequently depositing during the progressive withdrawal-induced drying process. The inset in Fig. 2(b) displays photographic documentation of the macroscopic film specimen, with substrate dimensions standardized at 1.5 cm × 1.5 cm. Figure 2(c) depicts the deposition morphology of self-assembled micelles fabricated via the dip-coating process. These were prepared from a 5 mg/mL THF solution at a withdrawal speed of 40 mm/min onto Si substrates coated with a 300-nm-thick SiO_2 layer. During substrate immersion and the subsequent dwell time in the dip-coating solution, rapid adsorption of unimers (free polymer chains) occurs [39]. This adsorption is driven by hydrogen bonding between the pyridine groups of the P4VP chains and the hydroxyl groups on the substrate surface. This results in the formation of a brush layer structure anchored to the substrate by the P4VP block, with the PS block extending into the solution. Subsequently, during substrate withdrawal, deposited micelles can be understood as those adsorbed onto the surface of this pre-formed brush layer because of the same PS composition. This configuration facilitates the adsorption of spherical micelles possessing a PS corona onto the substrate surface. Owing to the uniform micelle size (Fig. 2(a) and Fig. S1 in the ESM) and their close-packing arrangement, the self-assembled micelles form an ordered patterning structure. Higher-magnification AFM imaging (Fig. 2(c)) directly reveals the spherical micelles exhibiting a two-dimensional short-range ordered hexagonal arrangement on the surface, with a center-to-center distance of approximately $D_{C\text{-}C}$ = 34 nm. The dense, ordered packing of these spherical micelles on the substrate thereby provides an effective template fabrication of AuNP arrays.

The fabrication of AuNP arrays employs a facile one-step point-to-point adsorption method. The substrate coated with the self-assembled spherical micelle template is immersed in an aqueous solution of citrate-stabilized AuNPs, enabling AuNP adsorption onto the substrate. Turkevich–Frens [51, 52] method-synthesized AuNPs exhibit an average dry-state diameter of D_{AuNP} = 15.22 ± 0.22 nm (Fig. S2(a) in the ESM), while their mean hydrodynamic diameter in aqueous solution, measured by DLS, is D_h = 32.11 ± 0.12 nm (Fig. 3(a)). Upon immersion of the micelle-coated substrate into the citrate-stabilized AuNP solution (pH = 5.7), the P4VP domains undergo protonation and interact electrostatically with the negatively charged AuNPs. Surface zeta potential measurements (−29.3 mV, Fig. S2(b) in the ESM) confirm the negative surface charge of AuNPs, originating from citrate ions used for stabilization during synthesis. In contrast, the PS corona of the micelles hinders the electrostatically adsorption. The layered structure of the spherical micelles ensures the thinnest PS coverage at their top surface. Despite the inherent hydrophobicity of PS, local rearrangement of the PS corona occurs in the acidic environment, facilitating partial protonation of the P4VP core (usually occurs in the upper part of the P4VP core) and thereby enabling AuNP adsorption onto the partially protonated P4VP regions. Figure 3(b) presents a schematic illustration delineating the point-to-point adsorption mechanism inherent to this process. Kelvin probe force microscopy (KPFM) measurements were conducted on both the micelle template and the AuNP-adsorbed composite film. As shown in Figs. 3(c) and 3(d), the surface potential of the film decreased by 0.079 V after AuNP adsorption. This decrease is attributed to the probable formation of ion pairs between the citrate ligands stabilizing the AuNPs and the protonated P4VP cores, which establishes a directional permanent dipole layer at the interface [53, 54]. GISAXS (Fig. 3(e)) in-plane scans reveal that the micelle template sample exhibits only one distinct peak at approximately 0.0174 $Å^{-1}$, indicating an in-plane periodicity of about 36.7 nm, which is consistent with the measured center-to-center distance of micelles (34.4 nm) in Fig. 2(c). Compared to the micelle template curve, the composite film curve exhibits two additional diffraction peaks. The peak width at 0.0174 $Å^{-1}$ shows almost no change, indicating that the adsorption of AuNPs largely preserves the original periodicity of the micelle template without inducing significant lattice expansion or contraction, and that the AuNPs have precisely replicated the periodicity of the template. However, the newly emerged higher-order diffraction peak is significantly broadened, suggesting the presence of structural disorder on a smaller length scale. Scanning electron microscopy (SEM) images (Fig. 3(f)) reveal the AuNP arrays possess high density, minimal aggregation, and high surface coverage. Owing to the size match between the AuNPs and the micelles (D_{AuNP} ~ 15 nm vs. D_{P4VP} ~ 20 nm, D_h ~32 nm vs. $D_{C\text{-}C}$ ~ 34 nm), the arrangement of AuNPs closely replicates the template structure via point-to-point adsorption, yielding a 2D short-range ordered hexagonal configuration (Fig. 3(g)). Fast Fourier transform (FFT) processing of the lower-magnification SEM results reveals a distinct diffuse ring pattern, while the FFT of the high-magnification SEM image shows clear diffraction spots. This further confirms the short-range ordered structure of the AuNP array, which is largely consistent

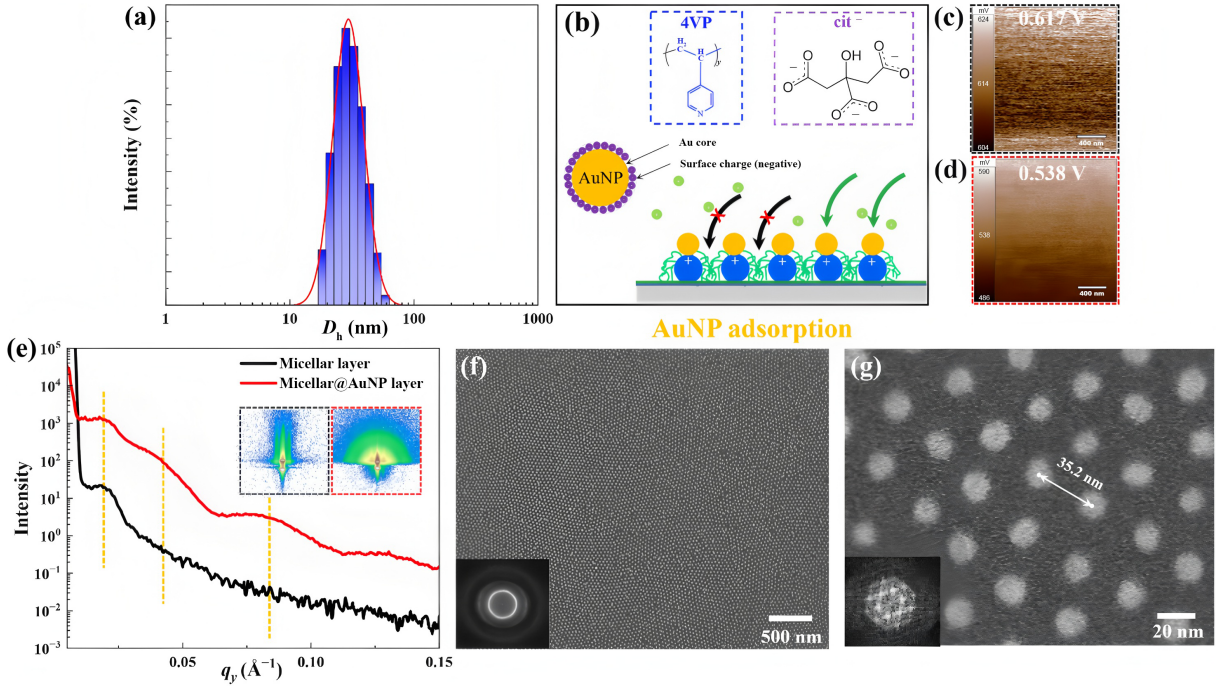

Figure 3 (a) The hydrodynamic diameter distribution of AuNPs determined by DLS. (b) Scheme of the micelle template-guided adsorption mechanism of AuNPs. (c) and (d) The surface potential test results of the spherical micelle template and the composite film after AuNP adsorption, respectively. (e) The GISAXS curves of the spherical micelle template and the composite film after AuNP adsorption. (f) and (g) The SEM images of AuNP arrays. The inset in (e) shows the 2D GISAXS patterns of the two films. The insets in (f) and (g) show the FFT results obtained using ImageJ.

with the grazing incidence small-angle X-ray scattering (GISAXS) results. Specifically, each 20-nm P4VP core accommodates a single 15-nm AuNP. Disruption of this size compatibility—for instance, by employing larger AuNPs—results in loss of the short-range ordered morphology, as demonstrated in Fig. S3 in the ESM. Collectively, we have successfully fabricated a NCP short-range ordered 2D AuNP array based on a BCP spherical micelle template using this simple and rapid method.

2.2 Effect of withdrawal rate on the morphology of deposited AuNPs

This morphological variance subsequently dictates the surface topography of the final AuNP assemblies. The substrate withdrawal speed exerts deterministic influences on the resultant micellar template morphology. Published articles have established a V-shaped relationship between withdrawal speed and polymer film thickness in dip-coating processes, where film thickness transitions from high to low and back to high as speed increases from slow to fast [55–58]. This distribution corresponds to three distinct regimes influenced by the interplay between withdrawal speed and solvent evaporation rate [56]. Figure 4(a) displays the thickness variation of self-assembled micelle template layers prepared from a 5 mg/mL solution at different withdrawal speeds, measured by spectroscopic ellipsometry. The template thickness still adheres to the V-shaped distribution. At low withdrawal speed (0.5 mm/min in this work), where the speed is significantly slower than the solvent evaporation rate, film deposition is dominated by solvent evaporation. At this slower withdrawal speed, rapid solvent evaporation at the three-phase contact line leads to near-instantaneous film formation upon substrate extraction. The abundance of spherical micelles in solution undergoes deposition without sufficient time for structural rearrangement due to the accelerated solvent evaporation, resulting in multilayered disordered packing morphology. Consequently, the ordering of AuNP adsorption is compromised by the multilayer micelle packing, exhibiting partially aggregated non-close-packed configurations (Fig. 4(b)).

As withdrawal speed increases toward the solvent evaporation rate (10 mm/min in this work, Fig. 4(c)), the liquid film thickness decreases due to viscous effects, placing overall film thickness near the minimum of the V-distribution. Here, withdrawal speed approaches the evaporation rate, reducing deposited micelle density below full surface coverage. Consequently, AuNP adsorption exhibits two distinct features: (i) Micelle deposition zones exhibit aggregated clusters with densely packed configurations, and (ii) sparse configurations with low packing density emerge through brush layer adsorption mediated by unassembled BCP chains. (Fig. 4(c)). Notably, a critical speed theoretically exists where micelle deposition ceases completely yielding minimal thickness contributed solely by the brush layer. Our results suggest the 10 mm/min condition lies beyond this critical minimum point, evidenced by sparse micelle deposition in AFM images (Figs. S4(a) and S5(b) in the ESM at 20 mm/min). At 30 mm/min, micelle deposition increases significantly (Fig. S4(b) in the ESM), with localized domains exhibiting ordered close-packing. Corresponding AuNP arrays display enhanced density and order (Fig. 4(d)). At 40 mm/min, near-optimal solvent evaporation-to-withdrawal speed matching occurs. AFM confirms near-complete surface coverage with large-area ordered close-packing (Fig. S4(c) in the ESM). This transitional regime exhibits rising thickness due to increasing micelle coverage. Crucially, the measured thickness (~ 20 nm) matches the P4VP core dimensions, confirming monolayer micelle deposition. At this velocity, solvent viscosity co-regulates micellar template deposition morphology on substrates, defining a transition regime. Monolayer micelle patterning is facilitated by kinetic matching between solvent viscosity and evaporation rate at

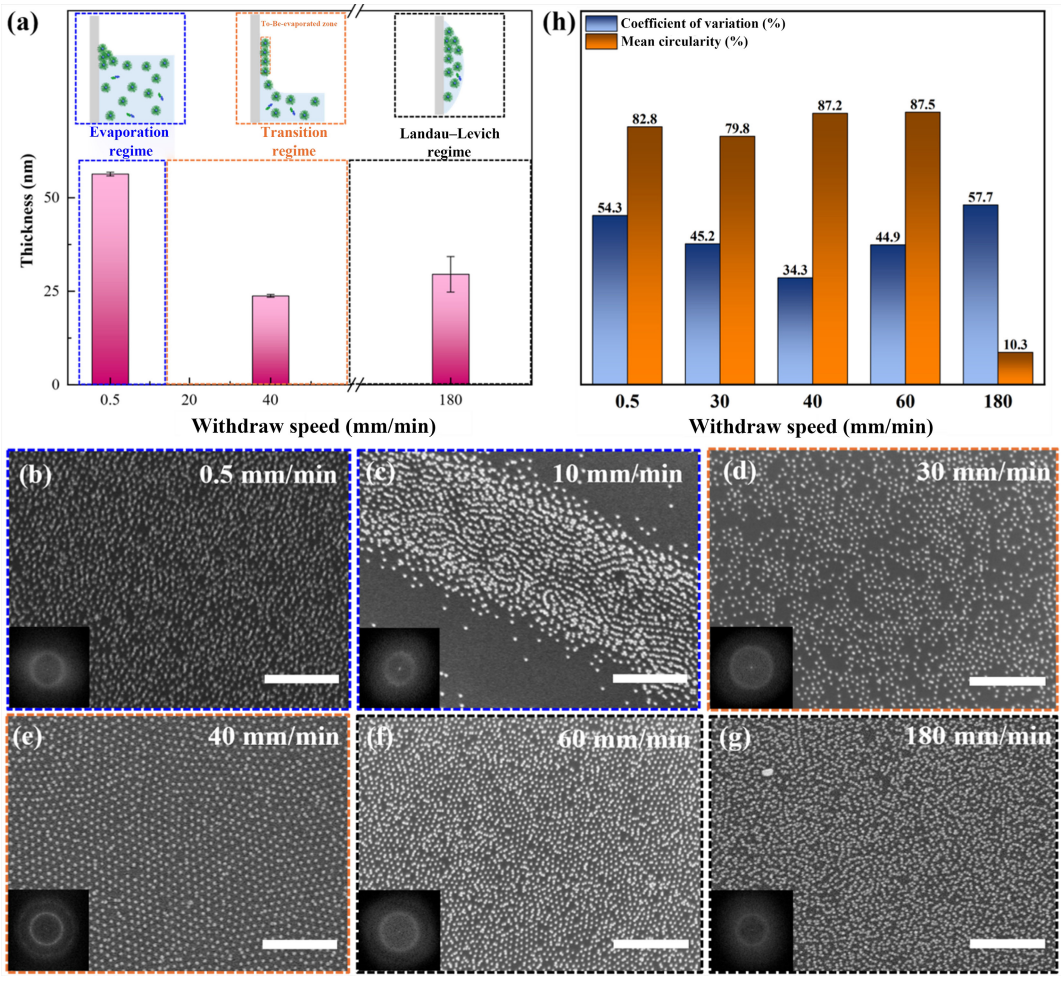

Figure 4 (a) Film thickness data measured by spectroscopic ellipsometry for three typical withdrawal speeds, along with schematic diagrams of liquid film profiles on the substrate surface during the withdrawal process at these speeds. (b)–(g) SEM micrographs of AuNPs on BCP micellar templats (prepared at the corresponding withdrawal speeds). (h) Histograms of the coefficient of variation in area and the mean circularity obtained after Voronoi tessellation of the SEM images of AuNPs on BCP micellar templates prepared at the corresponding withdrawal speeds. The inset images in (b)–(g) are FFT images processed using ImageJ.

40 mm/min withdrawal speed. This dynamic balance creates a to-be-evaporated zone with reduced thickness during substrate retraction, geometrically constraining particle assembly to vertical stacking of individual spherical micelles. Concurrently, PS-dominated corona properties induce interfacial avoidance behavior at solution-air interfaces, driving preferential adsorption near PS-enriched domains of BCP brush layers. This dual mechanism enables the formation of close-packed monolayer micellar arrays. Consequently, AuNP adsorption replicates this template, generating large-area, short-range ordered arrays with minimal aggregation (Fig. 4(e) and Fig. S4(c) in the ESM). A gradual increase in the withdrawal speed induces a morphological transition of micelles on the substrate surface from a multilayer stacked structure to a monolayer close-packed arrangement, accompanied by a corresponding decrease in film thickness. When the withdrawal speed matches the solvent evaporation rate, the micelles on the substrate surface adopt a monolayer close-packed morphology. The emergence of this close-packed configuration of spherical micelles constitutes a critical factor enabling the subsequent formation of short-range ordered arrangements in adsorbed AuNPs.

When the withdrawal speed further increases beyond the solvent evaporation rate, the film thickness on the substrate surface does not decrease further; instead, owing to the viscous effects of the solvent, the substrate surface retains a residual liquid film upon emerging from the solution, resulting in an increase in film thickness. At higher withdrawal speeds (60 and 180 mm/min in this work), Fig. S4(d) in the ESM reveals the onset of partial micelle stacking, indicating that the withdrawal speed now significantly exceeds the solvent evaporation rate (Fig. S5(d) in the ESM and Fig. 4(f)). This marks entry into the Landau-Levich regime, where solvent viscosity becomes the dominant factor governing deposition morphology [42]. Although increased withdrawal speed enhances micelle deposition quantity, complete second-layer formation is hindered. Secondary micelles adhere to the PS chain aggregation zones on the first-layer corona via the minimum surface energy principle, increasing overall film thickness. SEM images (Fig. 4(f)) show AuNP adsorption exhibiting dual morphologies: 2D short-range ordered non-close-packed configuration and multiply aggregated disordered packing. The main reasons for these two different morphologies are as follows: (i) Deposition positions of secondary micelles disrupt the ordered array guided by the underlying template; (ii) low PS molecular weight enables unstacked secondary micelles to undergo enhanced protonation of P4VP cores, increasing adsorption sites and allowing AuNP attachment beyond micelle tops. This effect intensifies at 180 mm/min (Fig. 4(g)), where the withdrawal speed far surpasses

evaporation, resulting in a fully wetted substrate upon withdrawal with minimal solvent loss. This resembles classical drop-casting, yielding highly irregular micelle templates devoid of large-area uniform order. In addition, Voronoi tessellation was performed on the SEM micrographs of the AuNP arrays in Fig. 4, and the Voronoi polygon areas and mean circularity were statistically analyzed to more intuitively reflect the orderliness of the AuNP arrays. The analysis results revealed that the AuNP array fabricated from the micellar template prepared at a withdrawal speed of 40 mm/min exhibited the lowest coefficient of variation in area and the highest mean circularity, indicating significantly superior orderliness compared to samples prepared at other withdrawal speeds, as shown in Figs. S6 and S7 in the ESM and Fig. 4(h). For BCP micelles, progressive solvent evaporation elevates residual solution concentration, destabilizing spherical micelles that were stable at the initial fixed concentration. Rod-like and amorphous micelle morphologies become prevalent, leading to uncontrollable AuNP adsorption patterns. It should be emphasized that adjusting the dip-coating withdrawal speed must be matched to the solvent's real-time evaporation rate under ambient conditions. While temperature and humidity significantly affect the solvent's evaporation kinetics, they do not influence the deposition of monolayer ordered micelle templates. Instead, they shift the optimal speed window for achieving such ordered monolayers earlier or later.

2.3 Effect of BCP solution concentration on the morphology of deposited AuNPs

In the following discussion, we demonstrated that effect of BCP concentration on morphology of template and AuNP deposits. The concentration of the BCP solution determines the morphology of micelle templates. For the PS-*b*-P4VP/THF system, solution concentration dictates micelle formation: Above the CMC, higher concentrations yield greater micelle content. As shown in Fig. S8(a) in the ESM, DLS measurements of solutions diluted from a 5 mg/mL stock confirm the CMC for PS_{24k}-*b*-$P4VP_{24k}$/THF is below 0.1 mg/mL, verifying spherical micelle presence even at our lowest coating concentration. Decreasing solution concentration increases the proportion of free unimers. The dynamic equilibrium between free BCP chains and spherical micelles maintains a low concentration of spherical micelles in solution. During substrate withdrawal from the solution, only limited micellar deposition occurred, yet this exhibited no measurable impact on subsequent AuNP adsorption density (Fig. S9 in the ESM). The low molecular weight of PS resulted in a relatively thin PS component within the deposited brush layer, which permitted sustained electrostatic adsorption of AuNPs by the underlying protonated P4VP layer. This phenomenon is corroborated by the SEM characterization presented in Fig. 5(a). The brush layer in this region also demonstrates AuNP adsorption capability (not point-to-point adsorption), though yielding nanostructures with disordered morphologies. Figures 5(a)–5(d) compares AuNP morphologies on templates prepared identically at 40 mm/min across four concentrations. Statistical data of AuNP areal density in Fig. 5 showed no significant variation among samples prepared at 0.1, 1, and 3 mg/mL concentrations. The observed effect is attributed to the brush layer on the substrate surface maintaining its AuNP adsorption capability even under conditions of diminished micellar content. However, SEM images revealed distinct morphological changes in AuNP arrangements, particularly when the concentration increased from 1 to 3 mg/mL. The observed structural evolution stems from distinct adsorption mechanisms between the brush layer and micellar assembly. While the brush layer facilitates stochastic AuNP adsorption, the micelle surface enables site-specific binding. Progressive concentration elevation induces denser micellar deposition, where closely packed micelles self-organize into ordered arrays, thereby templating the AuNP alignment toward enhanced positional regularity.

The mechanism of AuNP adsorption onto brush layers has been described in published works [59, 60]. It is noteworthy that this adsorption is closely related to the molecular weight of the PS block in the BCP used. When the PS molecular weight exceeds 50k, an excessively thick surface PS domain prevents most protons from penetrating, resulting in very low AuNP adsorption [58]. Another contributing factor may arise from the spatial isolation of

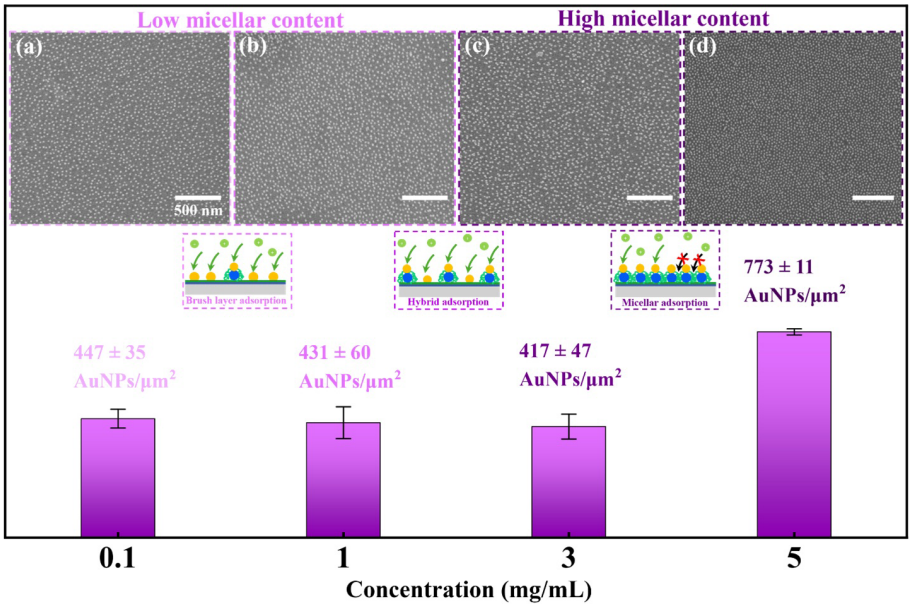

Figure 5 The adsorption density of AuNPs automatically quantified by ImageJ, with three measurements averaged per sample. (a)–(d) are the SEM micrographs of AuNP adsorption morphologies under four distinct BCP concentrations.

protonated, positively charged P4VP domains by thicker PS layers, which necessitates stronger electrostatic driving forces for large-scale AuNP adsorption. To test this hypothesis, we investigated BCPs with higher PS molecular weights (PS_{51k}-*b*-$P4VP_{18k}$) using identical experimental protocols. DLS data in Fig. S10(a) in the ESM confirms that the THF solution of PS_{51k}-*b*-$P4VP_{18k}$ at 0.1 mg/mL remains above the critical micelle concentration, indicating the continued presence of a certain number of spherical micelles in the solution. Figure 6 presents the AFM surface morphology of micelle template layers prepared using THF solutions of PS_{51k}-*b*-$P4VP_{18k}$ at different concentrations as the dip-coating solution with a withdrawal speed of 40 mm/min, along with the surface morphology after subsequent AuNP adsorption. The increase in PS molecular weight significantly expanded the interparticle core-to-core distance of spherical micellar templates.

Compared to the spherical micellar templates fabricated from the PS_{24k}-*b*-$P4VP_{24k}$ solution with equivalent close-packing at 5 mg/mL concentration, the interparticle core-to-core distance increased from 34.4 to 48 nm, whereas P4VP molecular weight variations induced negligible differences in micelle core dimensions. This spacing alteration led to reduced AuNP adsorption density and compromised array pattern definition when using such templates for subsequent nanoparticle deposition. SEM results clearly show AuNP adsorption onto the micelles. At a concentration of 0.1 mg/mL, the deposited layer exhibits an extremely low density of observable spherical micelles. At this stage, the deposit primarily consists of a brush layer formed by the adsorption of molecular chains. AuNP selective adsorption occurs only sporadically on top of isolated micelles; the 51k PS molecular weight almost completely blocks AuNP adsorption onto the brush layer (Figs. 6(a) and 6(e)). The observed phenomenon likely originates from the deposition mechanism of the brush layer. Free BCP chains forming the brush layer undergo hydrogen bonding interactions between protonated pyridyl N groups and the SiO_2 substrate, resulting in planar deposition. When the substrate immersed in weakly acidic AuNP aqueous solution, these loosely distributed protonated pyridyl N groups fail to provide sufficient electrostatic attraction for negatively charged AuNP adsorption [61, 62]. This limitation, however, is overcome in spherical micelle architectures through highly concentrated P4VP domains. The collapsed

P4VP core generates intense electrostatic forces upon protonation, enabling AuNPs to penetrate the thick PS corona and adhere to the micellar surface. When the solution concentration rises to 1 mg/mL, a noticeable increase in the number of surface micelle structures is observed. However, the relatively low micelle content still results in large inter-micelle spacing and relatively loose packing (Figs. 6(b) and 6(f). The PS segments between micelle cores do not collapse densely onto the P4VP core surfaces during solution drying due to this loose arrangement, failing to form a continuous, compact PS domain. Consequently, AFM reveals larger apparent micelle sizes due to these two factors. AuNP adsorption at this stage is entirely contributed by the spherical micelles. The matching size between AuNPs and the P4VP cores results in a one-to-one correspondence in adsorption. Virtually no AuNP adsorption is observed on the brush layer. When the concentration is increased to 5 mg/mL, we observe via AFM a closely packed two-dimensional self-assembled micelle template structure similar to that formed by the 24k molecular weight BCP. This template achieves the highest AuNP adsorption density of 621 ± 32 AuNPs/μm^2 (Figs. 6(d) and 6(h)). However, the larger PS molecular weight

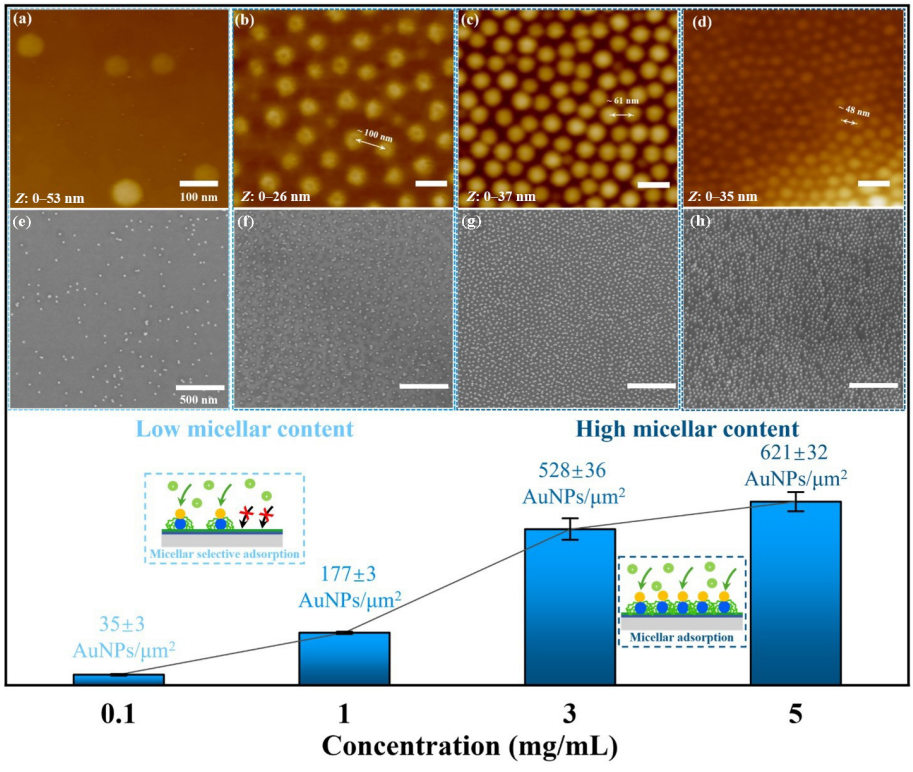

Figure 6 (a)–(d) AFM height images of BCP micelle templates prepared from 0.1, 1, 3, and 5 mg/mL PS51k-b-P4VP18k THF solutions at a withdrawal speed of 40 mm/min. The annotations in (b), (c) and (d) represent the average center-to-center distances between adjacent spherical micelles, obtained by statistically analyzing over 50 datasets. (e)–(h) SEM micrographs illustrating the morphologies of in situ adsorbed AuNPs under corresponding concentration conditions. The adsorption density of AuNPs was automatically quantified by ImageJ, with three measurements averaged per sample.

leads to significantly greater micelle core spacing compared to the 24k molecular weight BCP, resulting in lower AuNP adsorption density and an indistinct array morphology.

2.4 The performance of AuNP arrays as nano-floating-gates for transistor memory

AuNPs can serve as charge storage sites in organic nano-floating-gate transistor memories due to their high work function and discrete distribution characteristics. The high work function of AuNPs enables the formation of deep potential wells, resulting in stable charge retention capability [63, 64]. As shown in Fig. 7(a), BCP spherical micelle@AuNP array was employed as the charge trapping layer in a bottom-gate/top-contact nano-floating-gate memory (NFGM) device. A Tips-pentacene/PS layer, fabricated according to a previously reported preparation strategy [18], was deposited atop the charge trapping layer to function as the active/tunneling composite layer. For comparison, a control device using only a monolayer of spherical micelles as the charge-trapping layer was prepared using the same method, to test and contrast the performance variations between the two device configurations. Representative transfer and output characteristics of both devices are presented in Fig. 7(d) and 7(e), which demonstrate typical p-type field-effect behavior. Transfer curves reveals that the BCP@AuNP device exhibits a threshold voltage of approximately −9 V. This represents a leftward shift of about 9 V. This suggests that the inherent trap density within its floating-gate layer is low, leading to a weaker screening effect and allowing the channel to be more easily turned on by the gate voltage. The current on/off ratio (3.8×10^3) and subthreshold swing (2.0 V/dec) are both superior to those of the BCP device (1.7×10^3 and 3.5 V/dec respectively). Concurrently, the maximum transconductance shows an approximate 3.5-fold enhancement, suggesting that the electrostatic adsorption of AuNPs enables a higher drive current under an equivalent gate bias while introducing fewer interfacial defects. Furthermore, a comparison of the output curves indicates that the BCP@AuNP device achieves an output current approximately 24% higher than that of the BCP device, along with a 31% greater transconductance in the linear region. This suggests more efficient charge carrier transport within the channel.

Reversible threshold voltage (V_{TH}) shifts were conducted to evaluate the charge-trapping capability of the NFGM with an ordered functional layer. The memory window is defined as the difference in V_{TH} between the programmed and erased states. For the BCP@AuNP device, after applying a gate voltage of −80 V for 1 s, the transfer curve shifted toward the negative voltage direction from its initial position, indicating hole trapping in the device. Subsequently, upon illuminating the device (applying 5.314 mW/cm² white light for 2 s), the transfer curve shifted back to its initial position, yielding a hole-trapping memory window of 28 V. Similarly, by applying 80 V under illumination for 2 s followed by a −20 V gate voltage for 1 s, an electron-trapping memory window of 26 V was achieved. In contrast, the BCP-only device exhibited a

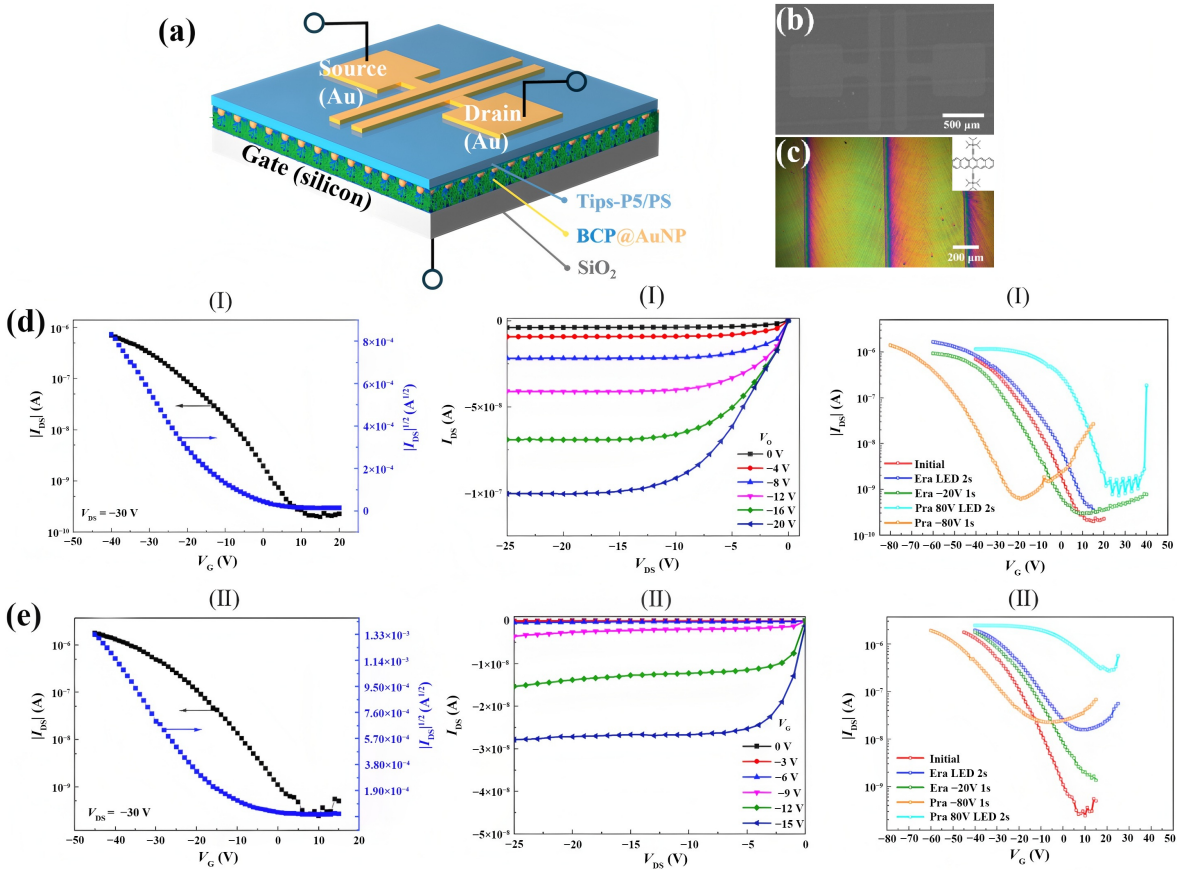

Figure 7 (a) Schematic diagram of the bottom-gate top-contact structured NFGM array. (b) SEM image of the source-drain electrodes and (c) microscope image of the Tips-Pentacene/PS layer. (d) and (e) The transfer characteristics, output characteristics, and programming (Pro)/Erasing (Era) threshold voltage transfer characteristic curves of the NFGM fabricated using two different floating-gate layers, respectively. The (I) marker above the images represents the device containing the AuNP array, while the (II) marker represents the device without AuNP.

hole-trapping window of 14 V and an electron-trapping window of 30 V. Both devices demonstrated bipolar trapping behavior for both holes and electrons. The introduction of AuNPs increased the overall memory window of the device by 10 V, while enhancing both hole- and electron-trapping capabilities. This phenomenon can be explained by the acidic aqueous conditions introduced during the AuNP adsorption process, which protonated the P4VP and enabled its binding to AuNPs via coordination interaction. The presence of this coordination structure provides additional active sites for charge trapping, which can act as electron donors or form local dipoles, thereby modulating the interfacial energy levels and stabilizing the trapped charges. Figure S11 in the ESM presents the write–read–erase–read (WRER) cycling curves under both hole-trapping and electron-trapping modes. For the device with adsorbed AuNPs, both hole and electron trapping remained stable (on/off ratio ≈ 10^2) even after 110 cycles. In comparison, the BCP-only device exhibited a slightly lower on/off ratio for hole trapping, while effective WRER cycling could not be achieved in electron-trapping mode.

3 Conclusion

In summary, we have developed a straightforward single-step dip-coating strategy to fabricate ordered 2D self-assembled BCP micelle templates on substrates and successfully generated 2D non-close-packed short-range ordered AuNP arrays through a point-to-point adsorption on these templates. Critical processing parameters, such as dip-coating speed and micelle concentration on the morphology of templates, and the effect of NP size and micelle shell thickness on electrostatic adsorption, were clarified to achieve large-area 2D non-close-packed NP arrays. The BCP@AuNP composite array demonstrates superior performance as a nano-floating-gate in non-volatile memory devices. Compared to the pure BCP micelle template layer, the incorporation of AuNPs leads to significantly enhanced memory window and improved operational stability. This strategy features simplicity, efficiency, versatility, and low cost, requiring no additional pretreatment or post-treatment steps. The entire process demonstrates significant potential for industrial-scale fabrication of controllable non-close-packed NP arrays.

Electronic Supplementary Material: Supplementary material (additional experimental details and characterization data: TEM/SEM/AFM images, DLS, zeta potential, Voronoi tessellation, and electrochemical cycling curves) is available in the online version of this article at https://doi.org/10.26599/NR.2026.94908645.

Data availability

All data needed to support the conclusions in the paper are presented in the manuscript and the Electronic Supplementary Material. Additional data related to this paper may be requested from the corresponding author upon request.

Acknowledgements

This work is granted by the National Natural Science Foundation of China (Nos. 52293474 and 52322314). The authors thank HUST Analytical and Testing Center and Core Facility of Life Science (HUST) for their support with the facilities.

Declaration of Competing Interest

All the contributing authors report no conflict of interest in this work.

Author contribution statement

C. X. L.: Conceptualization, methodology, investigation, formal analysis, data curation, writing – original draft, writing – review & editing, visualization. H. H. C investigation (partial data acquisition), writing – original draft (partial). S. D., W. L. (Wang Li) and X. M.: Methodology (partial). W. L. (Wen Li): Writing – review & editing. M. D. Y: Resources; R. H. D: Conceptualization, methodology, supervision, project administration, writing – review & editing. J. T. Z: Supervision, writing – review & editing, resources, funding acquisition.

Use of AI statement

None.

References

[1] Schmudde, M.; Grunewald, C.; Goroncy, C.; Noufele, C. N.; Stein, B.; Risse, T.; Graf, C. Controlling the interaction and non-close-packed arrangement of nanoparticles on large areas. *ACS Nano* **2016**, *10*, 3525–3535.

[2] Kim, S. J.; Park, Y. S.; Lyu, S. H.; Lee, J. S. Nonvolatile nano-floating gate memory devices based on pentacene semiconductors and organic tunneling insulator layers. *Appl. Phys. Lett.* **2010**, *96*, 033302.

[3] Li, W.; Sun, K.; Yang, L. S.; Mao, X.; Deng, S.; Jiang, H.; Gu, P.; Cao, B. W.; Li, W.; Yi, M. D. et al. *In situ* self-assembly of nanoscale particles into macroscale ordered monolayers with enhanced memory performance. *Small* **2023**, *19*, 2207468.

[4] Wang, K.; Ling, H. F.; Bao, Y.; Yang, M. T.; Yang, Y.; Hussain, M.; Wang, H. Y.; Zhang, L. B.; Xie, L. H.; Yi, M. D. et al. A centimeter-scale inorganic nanoparticle superlattice monolayer with non-close-packing and its high performance in memory devices. *Adv. Mater.* **2018**, *30*, 1800595.

[5] Yang, F.; Chen, Q. Y.; Wang, J. J.; Chang, J. J.; Dong, W. H.; Cao, W.; Ye, S. S.; Shi, L.; Nie, Z. H. Fabrication of centimeter-scale plasmonic nanoparticle arrays with ultranarrow surface lattice resonances. *ACS Nano* **2023**, *17*, 725–734.

[6] Liu, S. M.; Yang, Y. H.; Yu, H.; Han, G. Q.; Xu, Y. H.; Zhang, M. M.; Cheng, Q. Y.; Li, W.; Yi, M. D.; Xu, J. P. et al. Liquid/liquid interfacial assembly of poly(methyl methacrylate)-grafted nanoparticles into superlattice monolayers and their application as floating gates for high performance memory. *ACS Appl. Mater. Interfaces* **2025**, *17*, 2513–2521.

[7] Mao, X.; Yang, Y. H.; Yu, H.; Li, W.; Zhao, W. Q.; Deng, S.; Jin, S. H.; Jiang, L. Z.; Liu, C. X.; Li, W. et al. Printable nanoparticle superlattice monolayer via interfacial assembly: Toward high-performance multilevel nanocrystals floating-gate memory. *Adv. Funct. Mater.* **2026**, *36*, e16885.

[8] Hung, C. C.; Chiu, Y. C.; Wu, H. C.; Lu, C.; Bouilhac, C.; Otsuka, I.; Halila, S.; Borsali, R.; Tung, S. H.; Chen, W. C. Conception of stretchable resistive memory devices based on nanostructure-controlled carbohydrate-*block*-polyisoprene block copolymers. *Adv. Funct. Mater.* **2017**, *27*, 1606161.

[9] Meseguer, F.; Fenollosa, R. Non-close packed colloidal crystals. *J. Mater. Chem.* **2005**, *15*, 4577–4580.

[10] Zheng, W. X.; Fu, X. W.; Murtaza, G.; Zhang, N.; Meng, Z. H.; Wu, L.; Qiu, L. L. A PDMS-encapsulated cylindrical non-closed-packed photonic crystals composite with Bragg-enhanced Fresnel reflectance for optical gain and spectral selection. *J. Colloid Interface Sci.* **2024**,

666, 639–647.

[11] Chang, K. Q.; Zhang, C.; Liu, T. X. A comprehensive review on fabrication and structural design of polymer composites for wearable pressure sensors. *Polym. Sci. Technol.* **2025**, *1*, 3–24.

[12] Liu, D. J.; Zhu, P. C.; Zhang, F. K.; Li, P. S.; Huang, W. H.; Li, C.; Han, N. N.; Mu, S. R.; Zhou, H.; Mao, Y. C. Intrinsically stretchable polymer semiconductor based electronic skin for multiple perceptions of force, temperature, and visible light. *Nano Res.* **2023**, *16*, 1196–1204.

[13] Yang, F.; Ye, S. S.; Dong, W. H.; Zheng, D.; Xia, Y. F.; Yi, C. L.; Tao, J.; Sun, C.; Zhang, L.; Wang, L. et al. Laser-scanning-guided assembly of quasi-3D patterned arrays of plasmonic dimers for information encryption. *Adv. Mater.* **2021**, *33*, 2100325.

[14] Weissman, J. M.; Sunkara, H. B.; Tse, A. S.; Asher, S. A. Thermally switchable periodicities and diffraction from mesoscopically ordered materials. *Science* **1996**, *274*, 959–963.

[15] Lin, S. Y.; Chow, E.; Hietala, V.; Villeneuve, P. R.; Joannopoulos, J. D. Experimental demonstration of guiding and bending of electromagnetic waves in a photonic crystal. *Science* **1998**, *282*, 274–276.

[16] Bonafos, C.; Carrada, M.; Benassayag, G.; Schamm-Chardon, S.; Groenen, J.; Paillard, V.; Pecassou, B.; Claverie, A.; Dimitrakis, P.; Kapetanakis, E. et al. Si and Ge nanocrystals for future memory devices. *Mater. Sci. Semicond. Process.* **2012**, *15*, 615–626.

[17] Han, S. T.; Zhou, Y.; Xu, Z. X.; Huang, L. B.; Yang, X. B.; Roy, V. A. L. Microcontact printing of ultrahigh density gold nanoparticle monolayer for flexible flash memories. *Adv. Mater.* **2012**, *24*, 3556–3561.

[18] Mao, X.; Yang, Y. H.; Yang, L. S.; Qian, H. W.; Li, W.; Zhao, W. Q.; Deng, S.; Jin, S. H.; Jiang, L. Z.; Liu, C. X. et al. Orthogonal printing of uniform nanocomposite monolayer and oriented organic semiconductor crystals for high-performance nano-crystal floating gate memory. *J. Colloid Interface Sci.* **2024**, *668*, 232–242.

[19] Zhao, X. Y.; Li, D. H.; Zhu, J.; Fan, Y. B.; Xu, J. Y.; Huang, X. Y.; Nie, Z. H.; Chen, D. Y. Stably grafting polymer brushes on both active and inert surfaces using tadpole-like single-chain particles with an interactive "head". *ACS Macro Lett.* **2024**, *13*, 882–888.

[20] Zhang, Y.; Li, M. Y.; Li, B.; Sheng, W. B. Surface functionalization with polymer brushes via surface-initiated atom transfer radical polymerization: Synthesis, applications, and current challenges. *Langmuir* **2024**, *40*, 5571–5589.

[21] Ye, J. Z.; Chen, Z. K.; Chen, W. W.; Zhao, Y.; Ding, C. P.; Huang, Y. J. Gold nanoparticles coated with silica shells as high-performance fluorescence nanoprobe. *ACS Appl. Nano Mater.* **2024**, *7*, 5543–5553.

[22] She, X. J.; Liu, C. H.; Sun, Q. J.; Gao, X.; Wang, S. D. Morphology control of tunneling dielectric towards high-performance organic field-effect transistor nonvolatile memory. *Org. Electron.* **2012**, *13*, 1908–1915.

[23] Li, Z. Q.; Guo, P.; Zhou, Y. G. Dip-pen nanolithography enabled functional nanomaterials and their applications. *Adv. Mater. Technol.* **2021**, *6*, 2000897.

[24] Jiang, L. Z.; Mao, X.; Liu, C. X.; Guo, X. D.; Deng, R. H.; Zhu, J. T. 2D superlattices via interfacial self-assembly of polymer-grafted Au nanoparticles. *Chem. Commun.* **2023**, *59*, 14223–14235.

[25] Kim, M. P.; Kang, D. J.; Jung, D. W.; Kannan, A. G.; Kim, K. H.; Ku, K. H.; Jang, S. G.; Chae, W. S.; Yi, G. R.; Kim, B. J. Gold-decorated block copolymer microspheres with controlled surface nanostructures. *ACS Nano* **2012**, *6*, 2750–2757.

[26] Xu, M.; Ku, K. H.; Lee, Y. J.; Kim, T.; Shin, J. J.; Kim, E. J.; Choi, S. H.; Yun, H.; Kim, B. J. Effect of polymer ligand conformation on the self-assembly of block copolymers and polymer-grafted nanoparticles within an evaporative emulsion. *Macromolecules* **2021**, *54*, 3084–3092.

[27] Yun, H.; Lee, Y. J.; Xu, M.; Lee, D. C.; Stein, G. E.; Kim, B. J. Softness- and size-dependent packing symmetries of polymer-grafted nanoparticles. *ACS Nano* **2020**, *14*, 9644–9651.

[28] Chen, H. X.; Mu, S. L.; Fang, L. P.; Shen, H. Z.; Zhang, J. H.; Yang, B. Polymer-assisted fabrication of gold nanoring arrays. *Nano Res.* **2017**, *10*, 3346–3357.

[29] Cushen, J. D.; Bates, C. M.; Rausch, E. L.; Dean, L. M.; Zhou, S. X.; Willson, C. G.; Ellison, C. J. Thin film self-assembly of poly(trimethylsilylstyrene-*b*-$_{D,L}$-lactide) with sub-10 nm domains. *Macromolecules* **2012**, *45*, 8722–8728.

[30] Hu, X. H.; Xiong, S. S. Fabrication of nanodevices through block copolymer self-assembly. *Front. Nanotechnol.* **2022**, *4*, 762996.

[31] Lohmüller, T.; Aydin, D.; Schwieder, M.; Morhard, C.; Louban, I.; Pacholski, C.; Spatz, J. P. Nanopatterning by block copolymer micelle nanolithography and bioinspired applications. *Biointerphases* **2011**, *6*, MR1–MR12.

[32] Discher, D. E.; Eisenberg, A. Polymer vesicles. *Science* **2002**, *297*, 967–973.

[33] Han, Y. Y.; Yu, H. Z.; Du, H. B.; Jiang, W. Effect of selective solvent addition rate on the pathways for spontaneous vesicle formation of ABA amphiphilic triblock copolymers. *J. Am. Chem. Soc.* **2010**, *132*, 1144–1150.

[34] Parshad, B.; Krishna; Kumari, M.; Kaushik, K.; Pan, Y. W.; Achazi, K.; Böttcher, C.; Haag, R.; Sharma, S. K. Study on the self-assembly and dual-stimuli-responsive behavior of multi-amphiphilic polymeric architectures. *Polym. Sci. Technol.* **2025**, *1*, 144–154.

[35] He, X. H.; Song, M.; Liang, H. J.; Pan, C. Y. Self-assembly of the symmetric diblock copolymer in a confined state: Monte Carlo simulation. *J. Chem. Phys.* **2001**, *114*, 10510–10513.

[36] Dinsmore, A. D.; Hsu, M. F.; Nikolaides, M. G.; Marquez, M.; Bausch, A. R.; Weitz, D. A. Colloidosomes: Selectively permeable capsules composed of colloidal particles. *Science* **2002**, *298*, 1006–1009.

[37] Choucair, A.; Eisenberg, A. Control of amphiphilic block copolymer morphologies using solution conditions. *Eur. Phys. J. E* **2003**, *10*, 37–44.

[38] Andersson Trojer, M.; Nordstierna, L.; Nordin, M.; Nydén, M.; Holmberg, K. Encapsulation of actives for sustained release. *Phys. Chem. Chem. Phys.* **2013**, *15*, 17727–17741.

[39] Vyhnalkova, R.; Müller, A. H. E.; Eisenberg, A. Control of morphology and corona composition in aggregates of mixtures of PS-*b*-PAA and PS-*b*-P4VP diblock copolymers: Effects of solvent, water content, and mixture composition. *Langmuir* **2014**, *30*, 13152–13163.

[40] Xu, J. P.; Wu, Y. Q.; Wang, K.; Shen, L.; Xie, X. L.; Zhu, J. T. The generation of polymeric nano-bowls through 3D confined assembly and disassembly. *Soft Matter* **2016**, *12*, 3683–3687.

[41] Deng, R. H.; Liang, F. X.; Li, W. K.; Liu, S. Q.; Liang, R. J.; Cai, M. L.; Yang, Z. Z.; Zhu, J. T. Shaping functional nano-objects by 3D confined supramolecular assembly. *Small* **2013**, *9*, 4099–4103.

[42] Leffler, V. B.; Mayr, L.; Paciok, P.; Du, H. C.; Dunin-Borkowski, R. E.; Dulle, M.; Förster, S. Controlled assembly of block copolymer coated nanoparticles in 2D arrays. *Angew. Chem., Int. Ed.* **2019**, *58*, 8541–8545.

[43] Yan, N.; Liu, X. J.; Zhu, J. T.; Zhu, Y. T.; Jiang, W. Well-ordered inorganic nanoparticle arrays directed by block copolymer nanosheets. *ACS Nano* **2019**, *13*, 6638–6646.

[44] Liu, C. X.; Duan, L. J.; Yan, N.; Jiang, W. Hybrid Janus nanotubes with tunable internal pore size disassembled from mesoporous block copolymer-based hybrid scaffolds. *Chin. J. Polym. Sci.* **2022**, *40*, 1165–1172.

[45] Cui, Y.; Zhu, H. Y.; Cai, J. D.; Qiu, H. B. Self-regulated co-assembly of soft and hard nanoparticles. *Nat. Commun.* **2021**, *12*, 5682.

[46] Yap, F. L.; Thoniyot, P.; Krishnan, S.; Krishnamoorthy, S. Nanoparticle cluster arrays for high-performance SERS through directed self-assembly on flat substrates and on optical fibers. *ACS Nano* **2012**, *6*, 2056–2070.

[47] Kim, S. S.; Sohn, B. H. Catalytic tailoring of large-area reduced graphene oxide by tunable arrays of Pt nanostructures synthesized from self-assembling diblock copolymers. *Carbon* **2016**, *107*,

124–131.
[48] Kim, H.; Lim, Y.; Kim, S.; Kim, S. S.; Sohn, B. H. Nanoscale arrangement of diblock copolymer micelles with Au nanorods. *Nanotechnology* **2014**, *25*, 455602.
[49] Ghoshal, T.; Shaw, M. T.; Holmes, J. D.; Morris, M. A. Development of a facile block copolymer method for creating hard mask patterns integrated into semiconductor manufacturing. *Nano Res.* **2016**, *9*, 3116–3128.
[50] Jeon, S. M.; Lee, S. H.; Yoo, S. I.; Sohn, B. H. Ordered complex nanostructures from bimodal self-assemblies of diblock copolymer micelles with solvent annealing. *Langmuir* **2011**, *27*, 12191–12196.
[51] Frens, G. Controlled nucleation for the regulation of the particle size in monodisperse gold suspensions. *Nat. Phys. Sci.* **1973**, *241*, 20–22.
[52] Turkevich, J.; Stevenson, P. C.; Hillier, J. A study of the nucleation and growth processes in the synthesis of colloidal gold. *Discuss. Faraday Soc.* **1951**, *11*, 55–75.
[53] Pertl, F.; Lenton, I. C. D.; Cramer, T.; Waitukaitis, S. No time for surface charge: How bulk conductivity hides charge patterns from Kelvin probe force microscopy in contact-electrified surfaces. *Phys. Rev. Lett.* **2025**, *135*, 146202.
[54] Rahimi, E.; Palacios-Corella, M.; Mol, A.; Pané, S.; Puigmartí-Luis, J. Kelvin probe force microscopy in bionanotechnology: Current advances and future perspectives. *Adv. Mater.*, in press, DOI: 10.1002/adma.202510671.
[55] Roland, S.; Prud'homme, R. E.; Bazuin, C. G. Morphology, thickness, and composition evolution in supramolecular block copolymer films over a wide range of dip-coating rates. *ACS Macro Lett.* **2012**, *1*, 973–976.
[56] Dey, M.; Doumenc, F.; Guerrier, B. Numerical simulation of dip-coating in the evaporative regime. *Eur. Phys. J. E* **2016**, *39*, 19.
[57] Roland, S.; Gamys, C. G.; Grosrenaud, J.; Boissé, S.; Pellerin, C.; Prud'homme, R. E.; Bazuin, C. G. Solvent influence on thickness, composition, and morphology variation with dip-coating rate in supramolecular PS-*b*-P4VP thin films. *Macromolecules* **2015**, *48*, 4823–4834.
[58] Le Berre, M.; Chen, Y.; Baigl, D. From convective assembly to Landau−Levich deposition of multilayered phospholipid films of controlled thickness. *Langmuir* **2009**, *25*, 2554–2557.
[59] Zhu, H.; Masson, J. F.; Bazuin, C. G. Monolayer arrays of Au nanoparticles on block copolymer brush films for optical devices and biosensors. *ACS Appl. Nano Mater.* **2024**, *7*, 5637–5651.
[60] Zhu, H.; Masson, J. F.; Bazuin, C. G. Monolayer arrays of nanoparticles on block copolymer brush films. *Langmuir* **2019**, *35*, 5114–5124.
[61] Takeuchi, K.; Ireland, P. M.; Webber, G. B.; Wanless, E. J.; Hayashi, M.; Sakabe, R.; Fujii, S. Electrostatic adsorption behaviors of polymer plates to a droplet. *Langmuir* **2023**, *39*, 9617–9626.
[62] Lloyd, J. A.; Ng, S. H.; Davis, T. J.; Gómez, D. E.; Bach, U. Size selective adsorption of gold nanoparticles by electrostatic assembly. *J. Phys. Chem. C* **2017**, *121*, 2437–2443.
[63] Liu, Z.; Lee, C.; Narayanan, V.; Pei, G.; Kan, E. C. Metal nanocrystal memories-part II: Electrical characteristics. *IEEE Trans. Electron Devices* **2002**, *49*, 1614–1622.
[64] Kang, M. J.; Khim, D.; Park, W. T.; Kim, J.; Kim, J.; Noh, Y. Y.; Baeg, K. J.; Kim, D. Y. Synergistic high charge-storage capacity for multi-level flexible organic flash memory. *Sci. Rep.* **2015**, *5*, 12299.